Modeling Reactive Wetting when Inertial Effects are Dominant

Daniel Wheeler, James A. Warren and William J. Boettinger[*]

Metallurgy Division, Materials Science and Engineering Laboratory,

National Institute of Standards and Technology, Gaithersburg, MD 20899, USA

(Dated: April 21, 2010)

Abstract

Recent experimental studies of molten metal droplets wetting high temperature reactive substrates have established that the majority of triple-line motion occurs when inertial effects are dominant. In light of these studies, this paper investigates wetting, spreading and substrate dissolution when inertial effects are dominant using a thermodynamically derived, diffuse interface model of a binary, three-phase material. The liquid-vapor transition is modeled using a van der Waals diffuse interface approach, while the solid-fluid transition is modeled using a phase field approach. The results from the simulations demonstrate an $O\left(t^{-1/2}\right)$ spreading rate during the inertial regime and oscillations in the triple-line position when the metal droplet transitions from inertial to diffusive spreading. It is found that the spreading extent is reduced as dissoution is enhanced by manipulation of the initial composition. The results from the model exhibit good qualitative and quantitative agreement with a number of recent experimental studies of high-temperature droplet spreading, particularly experiments of copper droplets spreading on silicon substrates. Analysis of the numerical data suggests that the extent and rate of spreading can be characterized by a plausible definition of instantaneous interface energies. Furthermore, observations of the entropy-production field determine that dissipation primarily occurs in the locality of the triple-line region during the inertial stage, but extends along the solid-liquid interface region during the diffusive stage.

---

[*]Electronic address: daniel.wheeler@nist.gov

I.   INTRODUCTION

The literature surrounding reactive wetting of metal alloys is overwhelmingly concerned with characterizing wetting, spreading and dissolution of droplets on substrates in systems for which inertial effects are not dominant or the majority of dissipation is assumed to be due to viscous forces [1–4]. In many respects this seems an entirely reasonable approach since the majority of experiments do not capture the early time behavior when inertial effects are dominant, but focus on the late-stage spreading when chemical-diffusion dominates and substrate dissolution occurs. Typically, experimental studies measure only slow spreading on the order of seconds or even minutes for millimeter-sized metal droplets consistent with diffusion-dominated spreading [1, 5–7]. However, a number of recent experiments [7–10] capture the rapid early-stage spreading and demonstrate consistency with inertial time scales [11]. These variations in experimental findings can be attributed to differences in substrate temperature, composition of the vapor phase influencing substrate oxidation, contact mechanisms between the substrate and molten droplet, camera shutter speed, as well as other factors [7]. An often important aspect of managing these factors is arresting the possible formation of a substrate ridge on which the triple line becomes attached, which can retard spreading considerably [5].

In typical studies, the spreading droplet is characterized in terms of a velocity versus contact angle relationship where the velocity is scaled using the instantaneous Capillary number, $Ca = U\nu/\gamma$, where U is the triple-line speed, ν is the liquid viscosity and γ is the liquid-vapor interface energy. Saiz et $al.$ postulated that the dissipation mechanism may not be due to viscous forces as previously understood [7, 12]. Clearly, in cases where the dissipation mechanism is not due to viscous effects, Ca is no longer a useful quantity for characterizing the spreading and an alternative parameter is required. An effective "triple-line friction" derived from molecular kinetics theory is suggested by Saiz et $al.$ that is independent of viscosity but still dependent on interface energy and the contact angle. A number of recent experimental studies [11] clearly show that a large proportion of the spreading is characterized entirely by the inertial time scale ($t_i = \sqrt{\rho R_0^3/\gamma}$, where ρ is the liquid density and R_0 is the drop radius) with $U \sim t^{-1/2}$, which is much faster than typical viscous spreading laws [13]. Furthermore, molecular dynamics studies of Ag-Ni and Ag-Cu systems seem to confirm the $t^{-1/2}$ dependence of the spreading rate even for

2

relatively small droplets (≈ 25 nm), which is close to the lower limit for observable inertial effects [14, 15]. During inertial spreading, the drop shape is highly non-spherical with $Re > 10$ ($Re = \rho R_0 U/\nu$) for a millimeter-sized metal droplet. Hocking and Davis [16] have demonstrated that there is no simple relationship between contact angle and velocity when the approach to equilibrium becomes oscillatory, which seems to be the case in a number of experimental and numerical studies of millimeter-sized droplets [8, 9, 17, 18].

This paper employs a diffuse interface method in order to analyze the issues surrounding the inertial spreading regime and dissipation mechanism discussed above. The diffuse interface approach implicitly includes a wide range of phenomena, such as Marangoni flow, and as such does not require an explicit relationship between spreading rate and contact angle [19]. The only previous use of a diffuse interface method for modeling reactive wetting clearly identifies two separate spreading regimes: an initial convective regime and a subsequent diffusive regime [2]. The convective regime is recognized to be viscous in nature due to the excellent agreement with standard viscous spreading laws. Further work by these authors [4] employed the same model to examine the effects of dissolution on spreading by first recovering the non-dissolutive hydrodynamic limit as a base state. In the convective regime they found the spreading to be independent of the diffusion coefficient, but accelerated in the diffusive regime as the diffusion coefficient is increased. This paper outlines a similar process using the initial liquid concentration to vary the driving force for dissolution, while maintaining a constant diffusion coefficient. The general consensus of the literature is that inertial spreading occurs more slowly in systems that exhibit dissolution than in immiscible systems that do not exhibit dissolution [1, 20]. However, this is contradicted by a number of experiments for saturated and pure liquids that show that the spreading can be on a similar time scale under certain experimental conditions [7, 9].

The work of Villanueva *et al.* [4] considers droplets that do not exhibit inertial effects due to the small drop size, which is limited by the requirement of having a narrow interface (≈ 1 nm). In contrast to Villanueva *et al.*, this work sacrifices the realistic interface width in an attempt to model a system that exhibits inertial effects. Due to the drop size restrictions, the inertial time scale used in Villanueva *et al.* is $t_i \approx 6 \times 10^{-11}$ s and the capillary time scale, $t_c \approx 2 \times 10^{-11}$ s where $t_c = \nu R_0/\gamma$. At these values, the extent of spreading during the inertial stage is limited and the characteristic inertial effects are suppressed by viscous forces. The Ohnesorge number, given by $Oh = t_c/t_i$, quantifies the magnitude of the inertial effects

3

($Oh \approx 1 \times 10^{-3}$ for a typical millimeter-sized metal droplet). Characteristic inertial effects, such as triple-line droplet oscillations and large droplet curvature variations, are reduced for $Oh > 0.01$ and eliminated for $Oh > 1$ [18]. In Villanueva *et al.*, $Oh \approx 0.3$ and in this work $Oh \approx 6 \times 10^{-3}$. Other important time scales include the phase field relaxation time scale, $t_\phi = \delta^2/\epsilon_\phi M_\phi$ and the chemical-diffusion time scale, $t_{\text{diff}} \propto \delta^2/D_l$ (the full definition is in Section IV), where δ is the interface width, ϵ_ϕ is the free energy gradient coefficient, M_ϕ is the phase field mobility and D_l is the liquid chemical-diffusion coefficient. In the present work, $t_\phi = 1 \times 10^{-9}$ s, which is an order of magnitude faster than the inertial time scale and thus does not impact medium and late stage inertial dynamics. In contrast, $t_{\text{diff}} = 1.9 \times 10^{-4}$ s, which is very slow and corresponds approximately to the time required for the solid-liquid interface to move a distance δ due to chemical diffusion.

Jacqmin makes an extensive study of the role of the diffusive interface method, specifically for a Cahn-Hilliard–van der Waals system (CHW), in relieving the stress singularity that occurs for classical sharp interface methods [19]. Since the interface is diffuse, the CHW does not require an explicit alteration to the no-slip boundary condition to allow for triple-line slip. Jacqmin demonstrates that the CHW has the same far field and macroscopic behavior as classical hydrodynamic models of slip. Thus, in diffuse interface models that include hydrodynamics there is no need to define a slip length. The interface width determines both an effective slip length and the concentration profiles within the diffuse interface associated with adsorption and desorption; these factors effect the evolution of the system in subtle ways. There is no exact expression relating interface width and the effective slip length, however, $\lambda = \delta/2R_0$ is suggested as a good rule of thumb in Ding and Spelt [17], where λ is the dimensionless effective slip length for a diffuse interface model. It is claimed that the slip length can be as large as 50 nm [21], which is close to the chosen interface width in the present work, although the drop radius is only 1 μm. The slip length is found by Ding and Spelt to influence the onset of oscillations that occur when the droplet transitions from the inertial stage to the diffusive stage. The critical value of Re for which oscillations occur is reduced with decreasing λ [16].

The code used for the numerical analysis in this paper is developed using the FiPy PDE solver [22]. Details of how to install FiPy as well as the reactive wetting code used here are given on the FiPy web site [23]. The numerical analysis and figures presented in this paper can be reproduced with the open source tools available. The underlying linear solvers and

parallel capabilities are provided by the Trilinos tool suite [24, 25].

In the following section the governing equations are presented along with a discussion of the associated dimensionless parameters. Results and analysis from the numerical solution of the governing equations outlined in Section II are presented in sections III and IV with varying initial conditions. Section III analyzes simulations with initial conditions that are designed to approximate the idealized hydrodynamic limit of droplet spreading, while Section IV examines the effects of including a chemical driving force for dissolution and ends with a discussion of the dissipation mechanism. Section V presents the conclusions. Appendix A derives the governing equations presented in section II, while Appendix B presents details of the numerical methods.

II. GOVERNING EQUATIONS

In this section, the final forms of the governing equations are presented along with the associated thermodynamic parameters and functions. The full derivation of the governing equations is described in Appendix A. As outlined in the introduction, the system consists of a three phase (solid, liquid and vapor) binary alloy. The liquid-vapor system is modeled as a two component van der Waals fluid, while the solid-fluid system is modeled with a classical phase field description. The density field acts as the order parameter for the liquid-vapor transition. Thus, the system is fully characterized by the spatio-temporal evolution of the mass density of component 1, ρ_1, the mass density of component 2, ρ_2, the phase field, ϕ, as well as the barycentric velocity field $\vec{u}$, as determined through the momentum equation. The three dimensional equations are reduced to to two dimensions by imposing cylindrical symmetry about $r = 0$ in Figure 2. The incompressible approximation is not made in this work for numerical reasons outlined in Appendix B; all the phases are compressible. The solid is modeled as a very viscous fluid as in previous phase field reactive wetting studies [2, 4]. As the total mass density, $\rho = \rho_1 + \rho_2$, appears so frequently in the equations, it is more convenient to use ρ and ρ_2 as the independent density variables. For economy in notation, we write spatial derivatives $\partial_i \equiv \partial/\partial x_i$, $\partial_i^2 \equiv \partial^2/\partial x_i^2$ and require that repeated indices are summed, unless otherwise indicated. Note that although the equations are solved with cylindrical symmetry, the equations are presented in the following Cartesian forms:

5

1. Continuity

$$\frac{\partial \rho}{\partial t} + \partial_j \left(\rho u_j \right) = 0. \tag{1}$$

2. Diffusion

$$\frac{\partial \rho_2}{\partial t} + \partial_j \left(\rho_2 u_j \right) = \partial_j \left(\frac{M}{T} \partial_j \left(\mu_2^{NC} - \mu_1^{NC} \right) \right). \tag{2}$$

3. Phase

$$\frac{\partial \phi}{\partial t} + u_j \partial_j \phi = \epsilon_\phi M_\phi \partial_j^2 \phi - \frac{M_\phi}{T} \frac{\partial f}{\partial \phi} \tag{3}$$

4. Momentum

$$\begin{aligned}
\frac{\partial \left(\rho u_i \right)}{\partial t} + \partial_j \left(\rho u_i u_j \right) &= \partial_j \left(\nu \left[\partial_j u_i + \partial_i u_j \right] \right) \\
&\quad - \rho_1 \partial_i \mu_1^{NC} - \rho_2 \partial_i \mu_2^{NC} + \left(\epsilon_\phi T \partial_j^2 \phi - \frac{\partial f}{\partial \phi} \right) \partial_i \phi
\end{aligned} \tag{4}$$

where u_i is a velocity component, T is the temperature and $M = \bar{M} \rho_1 \rho_2 / \rho^2$ is the chemical mobility, which is proportional to the diffusivity, D, as outlined in Eq. (12). The values of $\bar{M}$ and ν vary from the solid to the fluid phases with the interpolation scheme chosen to be,

$$\bar{M} = \bar{M}_s^\psi \bar{M}_f^{1-\psi} \tag{5}$$

and

$$\nu = \nu_s^\psi \nu_f^{1-\psi} \tag{6}$$

where $\psi = \phi^a$ with $a = 4$. The values used in the simulations for $\bar{M}_s$, $\bar{M}_f$, ν_s and ν_f are in Table I. The choice of a is discussed in Section IV. The free energy per unit volume is postulated to have the form [26],

$$f = p \left(\phi \right) f_s + \left(1 - p \left(\phi \right) \right) f_f + W \phi^2 \left(1 - \phi \right)^2$$

where W is the phase field barrier height and $p(\phi) = \phi^3(10 - 15\phi + 6\phi^2)$ represents a smoothed step function common in phase field models [27]. The free energies per unit volume in the separate fluid and solid phases are given by,

$$f_f = \frac{e_1 \rho_1^2}{m^2} + \frac{e_{12} \rho_1 \rho_2}{m^2} + \frac{e_2 \rho_2^2}{m^2} + \frac{RT}{m} \left[\rho_1 \ln \rho_1 + \rho_2 \ln \rho_2 - \rho \ln (m - \bar{v}\rho) \right]$$

and

$$f_s = \frac{A_1 \rho_1}{m} + \frac{A_2 \rho_2}{m} + \frac{RT}{m} \left(\rho_1 \ln \rho_1 + \rho_2 \ln \rho_2 - \rho \ln \rho \right) + \frac{B}{\rho m} \left(\rho_s^{\text{ref}} - \rho \right)^2 \tag{7}$$

where m is the molecular weight (assumed to be equal for each component), R is the gas constant, $\bar{v}$ is the exclusion volume due to the finite size of the atoms, B is the solid compressibility, ρ_s^{ref} is a reference density for the solid and the $e_i \rho_i / m$ are the free energy contributions per unit mole due to intermolecular attraction in the van der Waals model. The A_1 and A_2 are temperature dependent parameters related to the heat of fusion between the solid and fluid phases. Along with the free energy, the specification of the non-classical chemical potentials and the pressure are required to fully define the system,

$$\mu_1^{NC} = \frac{\partial f}{\partial \rho_1} - \epsilon_1 T \partial_j^2 \rho_1 \tag{8}$$

$$\mu_2^{NC} = \frac{\partial f}{\partial \rho_2} - \epsilon_2 T \partial_j^2 \rho_2 \tag{9}$$

$$P = \rho_1 \frac{\partial f}{\partial \rho_1} + \rho_2 \frac{\partial f}{\partial \rho_2} - f \tag{10}$$

where ϵ_1 and ϵ_2 are free energy gradient coefficients. The parameter values for the system of equation above are presented in Table I. The corresponding isothermal phase diagram for the molar fraction of component 1 verses the molar volume is displayed in Figure 1.

Eqs. (1)–(4) are solved using a cell-centered, collocated finite-volume (FV) scheme. The solution algorithm uses a fully coupled Krylov solver with Picard non-linear updates using ρ_1, ρ_2, ϕ and $\vec{u}$ as the independent variables. Further discussion of the numerical approach is given in Appendix B.

A. The Dimensionless Form of the Equations

It is useful for discussion and analysis to recast in a dimensionless form Eqs. (2) and (4) for the liquid phase. They are respectively,

$$\frac{\partial \rho_2}{\partial t} + \partial_j (u_j \rho_2) = \frac{1}{Pe} \partial_j \left(\frac{\rho_1 \rho_2}{\rho^2} \partial_j \left(\mu_2 - \mu_1 - I \partial_k^2 (\rho_2 - \rho_1) \right) \right) \tag{11}$$
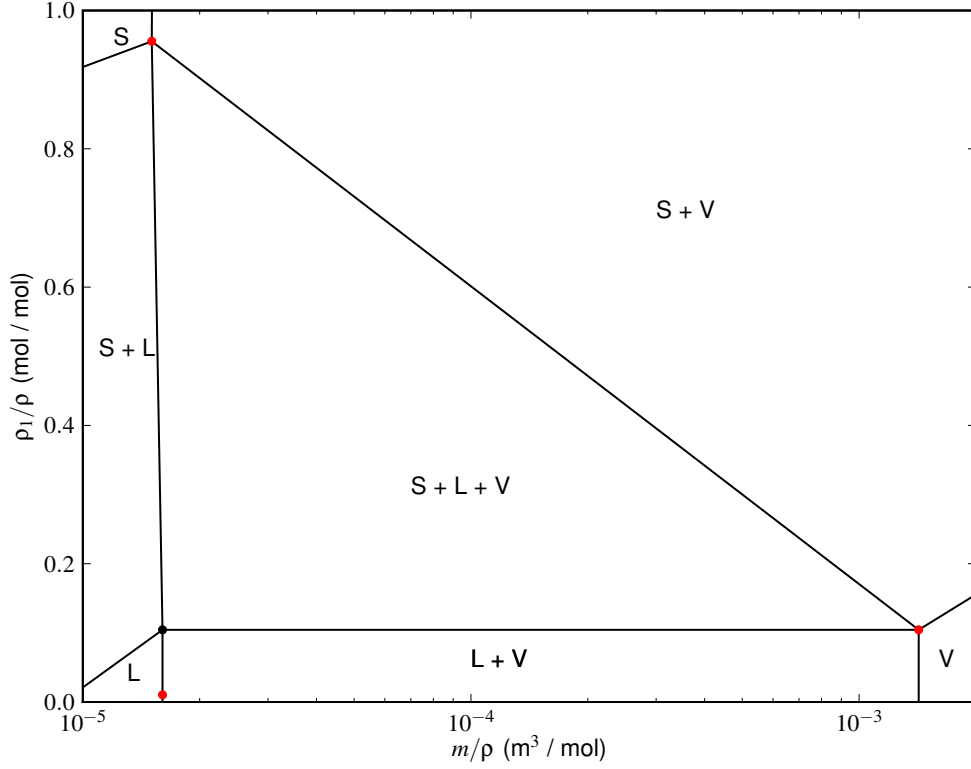
FIG. 1: The phase diagram for the system of parameters presented in Table I. Each region repre-
sents a possible equilibrium state for a mixture of solid (S), liquid (L) and vapor (V) phases. The
red dots represent the initial conditions for the $\xi = 0.1$ simulation discussed in Section IV. The
black dot marks the liquid equilibrium condition.

and

$$\frac{\partial \left(\rho u_i\right)}{\partial t} + \partial_j \left(\rho u_i u_j\right) = \frac{1}{Re}\partial_j \left(\partial_j u_i + \partial_i u_j\right) - \frac{1}{Ma^2}\partial_i P + \frac{1}{We} \left(\rho_k \partial_i \partial_j^2 \rho_k - \tilde{\epsilon}_\phi \partial_i \phi \partial_j^2 \phi\right)$$

where the variables and operators are now dimensionless. The dimensionless numbers
(Reynolds number, Mach number, Weber number and Peclet number) are defined by

$$Re = \frac{U R_0 \bar{\rho}}{\nu}$$
$$Ma = \frac{U}{c}$$
$$We = Re\,Ca$$
$$Pe = \frac{U \bar{\rho} R_0 m}{\bar{M} R}$$

8

Parameter	Value	Unit
ν_f	$2.0{\times}10^{-3}$	$\mathrm{kg/(s \cdot m)}$
ν_s	$2.0{\times}10^{4}$	$\mathrm{kg/(s \cdot m)}$
ϵ_1	$2.0{\times}10^{-16}$	$\mathrm{m^7/(K \cdot kg \cdot s^2)}$
ϵ_2	$2.0{\times}10^{-16}$	$\mathrm{m^7/(K \cdot kg \cdot s^2)}$
T	$6.5{\times}10^{2}$	K
m	$1.18{\times}10^{-1}$	$\mathrm{kg/mol}$
R	8.31	$\mathrm{J/(K \cdot mol)}$
v_a	1.0	
e_1	$\text{-}4.56{\times}10^{-1}$	$\mathrm{J \cdot m^3//mol^2}$
e_2	$\text{-}4.56{\times}10^{-1}$	$\mathrm{J \cdot m^3//mol^2}$
$\bar{v}$	$1.3{\times}10^{-5}$	$\mathrm{m^3/mol}$
A_1	$2.83{\times}10^{4}$	$\mathrm{J/mol}$
A_2	$5.64{\times}10^{4}$	$\mathrm{J/mol}$
ρ_s^{ref}	$7.84{\times}10^{-5}$	$\mathrm{kg/m^3}$
B	$2.02{\times}10^{5}$	$\mathrm{J/mol}$
W	$1.27{\times}10^{5}$	$\mathrm{N/m^2}$
ϵ_ϕ	$1.0{\times}10^{-9}$	$\mathrm{N/K}$
M_ϕ	$1.0{\times}10^{4}$	$\mathrm{K \cdot m^2/(N \cdot s)}$
$\bar{M}_f$	$1.0{\times}10^{-7}$	$\mathrm{kg \cdot s \cdot K/m^3}$
$\bar{M}_s$	$1.0{\times}10^{-11}$	$\mathrm{kg \cdot s \cdot K/m^3}$

TABLE I: Base parameter set

Note that the expression,

$$D = \frac{\bar{M}R}{m\bar{\rho}} \tag{12}$$

is the chemical-diffusion coefficient. The dimensionless number I is defined to be,

$$I = \frac{m\gamma}{RT\bar{\rho}R_0}$$

and represents the ratio between interface and internal forces in the liquid droplet. The system scalings are selected so that the dimensionless numbers reflect the relative influence of terms in the equations. The reference density $\bar{\rho}$ is the liquid equilibrium density indicated

9

in the phase diagram by the black dot (Figure 1). An additional useful quantity is the speed
of sound in the liquid [28], which is given by,

$$c = \sqrt{\frac{\partial P}{\partial \rho}}\bigg|_{\bar{\rho}}$$

III. HYDRODYNAMIC SPREADING

This section presents results for a number of simulations that aim to approximate the
hydrodynamic limit of droplet spreading, i.e. where surface tension forcing dominates and
interface motion is due to convection as phase change is negligible. The simulations per-
formed in this section provide a base state for comparison with the simulations performed
in Section IV that include a chemical driving force for dissolution. In the hydrodynamic
limit, comparisons can be made with traditional spreading models and power laws, but now
including the full detail of the flow patterns and compositional evolution. Interestingly, and
unlike in previous reactive wetting models [1, 2], this work considers spreading when $Oh \ll 1$,
where we are reminded that $Oh = t_c/t_i = \nu/\sqrt{R_0\rho\gamma}$. In this limit the interface energy and
inertial forces dominate over viscous effects, which represents a more realistic physical limit
for larger droplets. For example, for a millimeter sized drop of copper $Oh \approx 2 \times 10^{-3}$, while
for a micron-sized drop of lead $Oh \approx 2 \times 10^{-2}$. The analysis of reactive droplets spreading
when $Oh \ll 1$ is presented in the next section.

The initial configuration for the base simulation consists of a spherical droplet with a
radius of 1 μm surrounded by a vapor and in contact with a solid substrate. The droplet
spreads to attain its equilibrium configuration. In order to approximate the hydrodynamic
limit, the initial concentration and density in each phase are chosen to be the nominal planar
equilibrium values from the phase diagram, see Figure 1. The model includes physical effects
that prove to be negligible for the initial conditions chosen and time scales of interest. These
effects include (i) the readjustment of the equilibrium liquid density and concentration due
to the Gibbs-Thomson effect, (ii) the hydrodynamic distortion of the contact region and
(iii) phase change in the contact region due to the vertical interface energy imbalance.
The parameter values and initial conditions for the base simulation are given in Table I.
In general, if the initial configuration of the field variables are chosen to be discontinuous
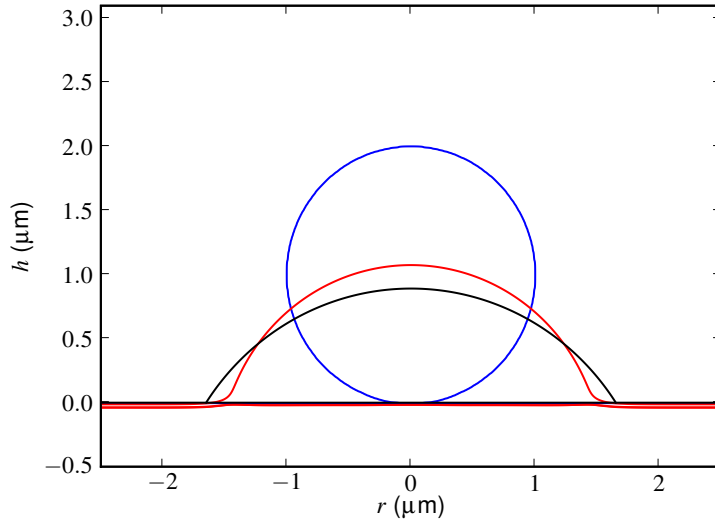between phases, the calculations become unstable and diverge. To avoid this, the field

FIG. 2: The contours $\phi = 0.5$ and $\rho = \rho_v^{\mathrm{equ}} + \left(\rho_l^{\mathrm{equ}} + \rho_v^{\mathrm{equ}}\right)/2$ indicate the solid-fluid and liquid-vapor interfaces respectively. The initial configuration is blue and the final equilibrium is red $(t/t_i \approx 70)$. The black curve shows the droplet shape obtained using an approximate technique discussed in the text.

variables are smoothed using a small diffusion step as part of the initialization procedure. Test simulations verify that the spreading rate is independent of the magnitude of the initial diffusion step below a given threshold.

Figure 2 shows the initial and final configuration of the droplet. Also shown (in black) is the final shape for an idealized situation where the initial volume fractions for each phase are conserved, the solid-fluid interface is flat and the contact angle of 0.32π rad is obtained by integrating the expression for the interface energy in Eq. (16) using results from planar equilibrium calculations. This is a reasonable approximation for the quasi-equilibrium droplet shape, as simulation results at $t \approx 70t_i$ show density variations of $\Delta\rho/\rho = 0.005$ in the interior of the liquid drop. In these simulations the behavior of the solid is approximated by a fluid with a high viscosity, which is a similar approach to that taken in previous work [2]. The solid viscosity, ν_s, is chosen such that $t_s = \delta\nu_s/\gamma \approx 2.7 \times 10^{-5}t_i$ where t_s represents the time scale for discernible motion of the solid due to hydrodynamics. Typically, for the hydrodynamic simulation the solid-fluid interface motion is less than $\delta/5$ for the duration of a simulation.

In the work of Ding and Spelt [17], phase field and level set models of a spreading droplet
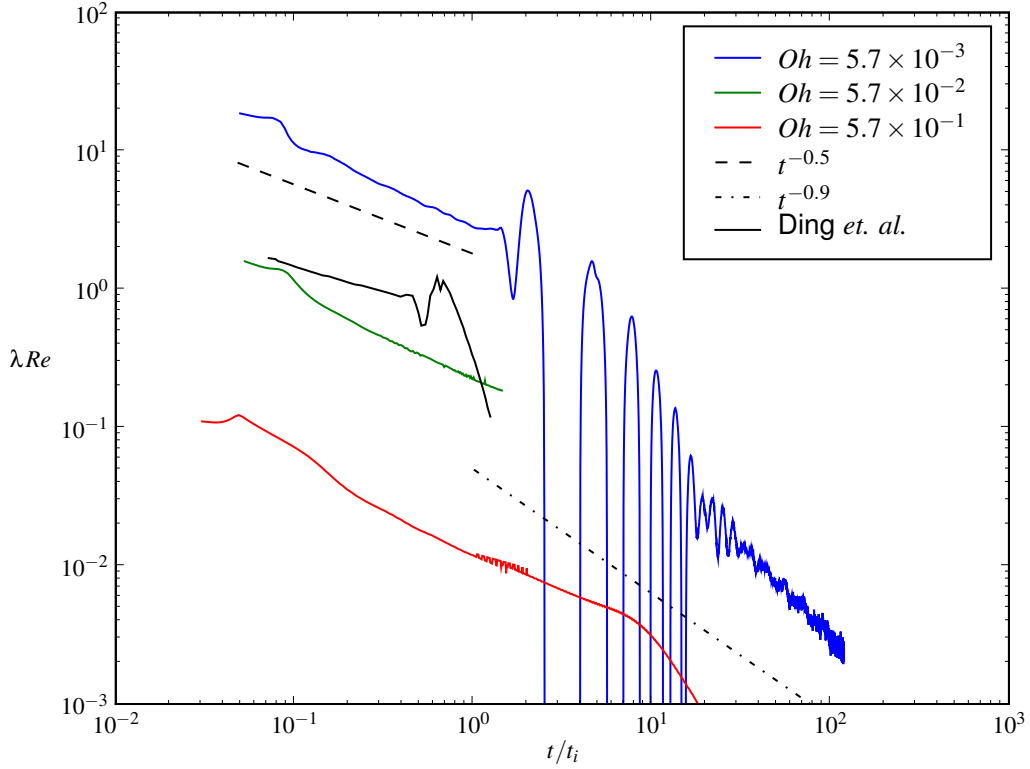
11

FIG. 3: The dimensionless spreading rate against the dimensionless time for the base simulation designed to approximate the hydrodynamic limit. The spreading occurs in two distinct regimes, the inertial regime when $t < t_i$ and the diffusive regime when $t > 10t_i$. The triple-line location is calculated using techniques similar to those presented in reference [4]. The sign changes in the blue curve correspond to the triple-line oscillations during the transition from the inertial to the diffusive regime.

were compared in the low Ohnesorge limit. Their work acts as a useful comparison for the simulations presented here. Ding and Spelt present their results using the inertial time scale, $t_i = \sqrt{\rho R_0^3/\gamma}$, and the dimensionless spreading rate, λRe, which in turn depends on both the effective dimensionless slip length $\lambda = \delta/2R_0$ and the Reynolds number, $Re = UR_0\rho/\nu$. Note that the Reynolds number requires specification of the instantaneous spreading rate U. Figure 3 displays the dimensionless spreading rate, λRe, against the dimensionless time t/t_i for simulations with varying Oh. The black curve in Figure 3 is a digitized curve from Ding and Spelt [17] representing the lowest value of Oh used in their work ($Oh = 0.00707$).

12

The calculation of triple-line velocities is necessarily noisy, with fluctuations on a timescale of $\Delta x/U$, where Δx is the fixed grid spacing. In Figure 3, the curves are constructed using a 20 point boxcar (equally-weighted) averaging scheme collected at every 10 time steps during the simulation. We note that the sign changes in the blue curve ($t_i < t < 10t_i$) correspond to the triple-line oscillations discussed below, and are *not* due to the averaging scheme. The velocity fluctuations will be small when U is large. Indeed, at early times, when $t/t_i < 1$, U is relatively large and the results are smooth. At later times, when $t/t_i > 10$, the averaging scheme does not smooth out the noise, as the spreading rate is greatly reduced, as can be seem in the noisy behavior at long times of the $Oh = 5.7 \times 10^{-3}$ curve (blue) in Figure 3. The noise in the low velocity regime of Figure 4 also reflects this behavior.

At early times, the flow is dominated by inertia and comparisons with theories of spreading on flat, non-reactive substrates are fruitful. Indeed, an analytical spreading rate for the inertial regime can be derived, see Biance *et al.* [13], and is given by $t^{-1/2}$. In Figure 3, the slope of this power law shows good agreement with the blue curve during the inertial regime. The height of the curve indicating the power law has be selected to enable easy comparison with the $Oh = 5.7 \times 10^{-3}$ (blue) curve. Furthermore, the classical Tanner's law for viscous spreading corresponding to $t^{-0.9}$ [13, 29] is also displayed for reference purposes. Oscillations, discussed below, complicate the analysis until $t \approx 10t_i$, as is seen in the $Oh = 5.7 \times 10^{-3}$ curve (blue).

Ding and Spelt simulated droplets that spread from an initial contact angle of $\pi/3$ rad to an equilibrium contact angle of $\pi/18$ rad using an effective dimensionless slip length of $\lambda = 0.01$. This is considerably different from the base simulation described here, however, most significantly the value of $Oh = 5.7 \times 10^{-3}$ used here is close to the smallest value used in their work. Since Ding and Spelt's choice of dimensionless spreading rate scales with λ, the choice of λ has a major impact on the height of the blue and black curves in Figure 3. For example, if $\lambda = 0.01$ as in Ding and Spelt's work, the blue and black curves coincide; however, this is equivalent to setting the effective slip length equal to the grid spacing and is thus too narrow. Previous publications have suggested that $\delta/2$ is a reasonable choice for the effective slip length in diffuse interface models [17, 19] and is used to calculate the value of λ for the curves in Figure 3. The relationship between interface width and effective slip length for diffuse interface models is an open topic of study and beyond the scope of this paper, see Jacqmin [19] for a discussion.
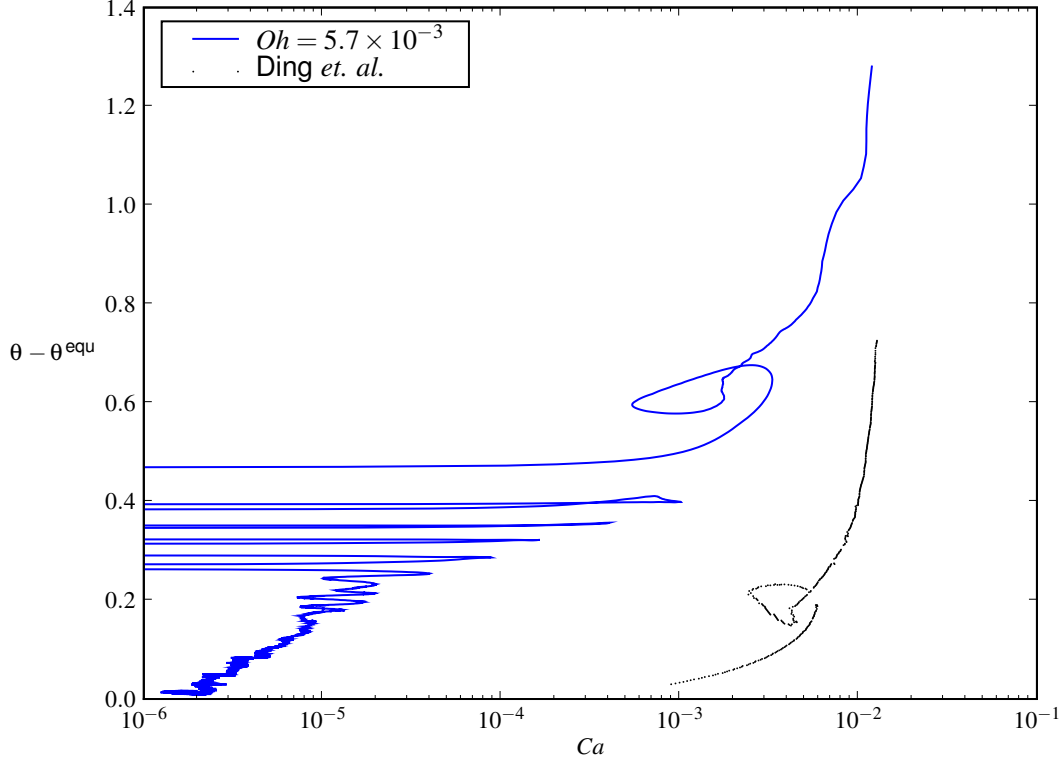
FIG. 4: The contact angle against Ca for the base simulation. The angle measurements are calculated using the tangent to the liquid-vapor interface at a distance of 1.3 δ from the triple-line location. In general, this distance results in good approximation to the apparent contact angle.

Figures 4 and 5 demonstrate the oscillatory nature of the drop motion during the inertial regime. The most noticeable feature of the spreading is a capillary wave that propagates from the triple-line along the liquid-vapor interface, initiating with the onset of the triple-line motion and progressing to the top of the droplet, causing a rapid rise in the drop height. The wave then travels back to the triple-line location while the droplet completes the majority of the spreading, with both events having a duration that corresponds to $\approx 2t_i$. Subsequent oscillations occur with a period of $\approx 2t_i$. During this process, the triple line motion and the drop height motion experience multiple changes of direction. The overall motion of the droplet agrees well with the qualitative descriptions noted in Ding and Spelt [17] for droplets simulated with a similar Ohnesorge number, although triple line motion was not seen to reverse direction in Ding and Spelt. In Figure 4, the contact angle experiences a
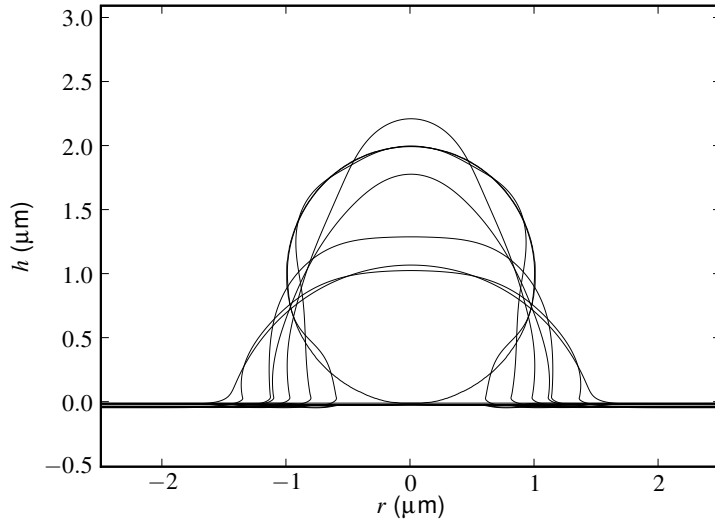
14

FIG. 5: Sequential configurations of the liquid-vapor and solid-liquid interfaces during the inertial regime. The curves demonstrate the extreme inertial effects on the droplet. The drop height rises up considerably as the capillary wave initiated from the triple line arrives at the top of the droplet. In the second-to-last sequential curve the drop height is below the final curve. Although large amplitude ($\approx R_0/5$) oscillations occur in the triple-line position, the largest contact angle oscillation is only $\approx 0.013\pi$ rad.

hysteresis loop in a similar fashion to the work of Ding and Spelt, which is reproduced in Figure 4.

In Figures 6 and 7 the spreading in the hydrodynamic base case is compared with experimental results from Saiz and Tomsia [7, 11] and Protsenko *et al.* [9] demonstrating remarkable agreement in time scale and suggesting that the experimental results are mostly inertial in nature. In the case of Saiz and Tomsia, the experimental results presented are for Au and Cu droplets of 1 mm spreading on metal substrates at high temperatures and predict much faster spreading than in similar high temperature experiments on other materials. Similarly, the results in Protsenko *et al.* predict fast spreading for Cu on Si. The experiments use the dispensed drop technique, which removes many complications such as melting, equilibration with the atmosphere, oxide skim removal, and, most importantly, it reduces the effect of the triple junction being attached to a ridge structure that may have hindered "true hydrodynamic" spreading in previous experiments. The reasonable quantitative agreement in Figures 6 and 7 (within $\approx 20\%$ for the Cu-Mo alloy) suggests that the
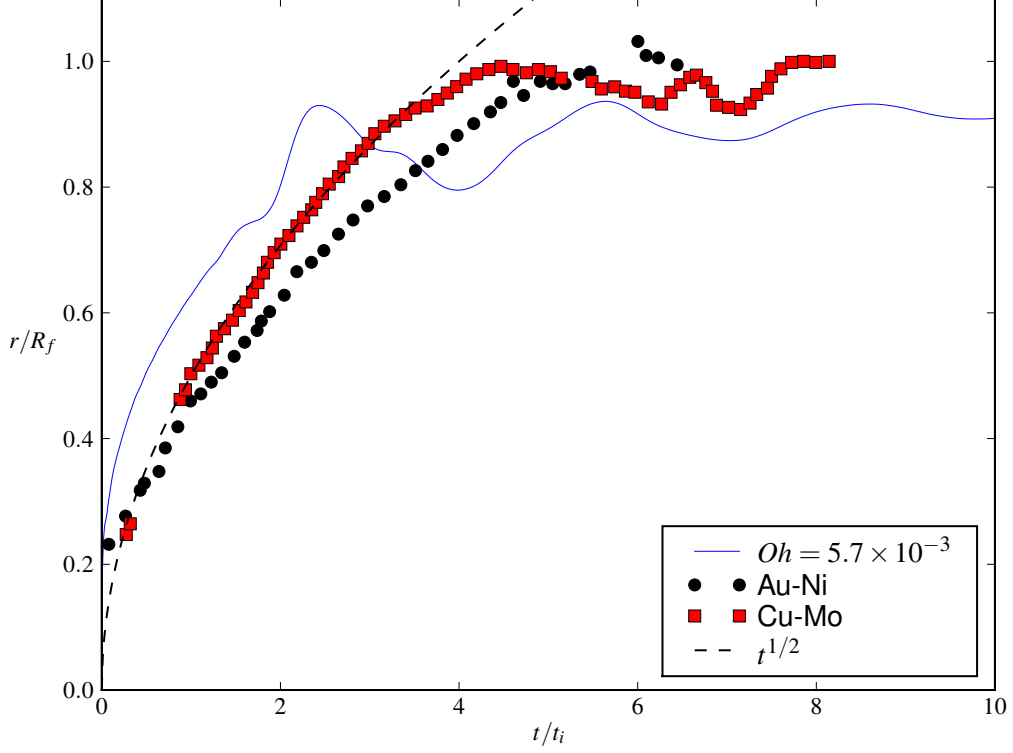
FIG. 6: The radial position of the triple line scaled against the final radial position, R_f, against time (scaled with t_i) for the base hydrodynamic case, Au-Ni experimental results and Cu-Mo experimental results. The experimental results are digitized from Saiz *et al.* [7, 11]. The inertial time scale, t_i for the Au-Ni system is calculated using $\rho = 1.1 \times 10^4$ kg/m^3, $\gamma = 1.0$ J/m^2, $R_0 = 1 \times 10^{-3}$ m. The inertial time scale for the Cu-Mo system is calculated using $\rho = 8.9 \times 10^3$ kg/m^3, $\gamma = 1.3$ J/m^2 and $R_0 = 1 \times 10^{-3}$ m. The value of t_i is 1.9×10^{-8} s for this work, 3.4×10^{-3} s for the Au-Ni system and 2.6×10^{-3} s for the Cu-Mo system. This figure shows the reasonable agreement between the simulation and experimental data when scaled by the inertial time scale and the agreement with the $t^{1/2}$ spreading rate.

spreading in the experimental systems is predominantly inertial in nature [11]. Other alloy combinations were also observed to have time scales consistent with the Au and Cu systems. The Cu spreading in Figure 6 also appears to indicate oscillatory behavior at the end of the inertial regime similar to the base case here. Since the period of the oscillations is $\approx 2t_i$, a much greater duration of experimental data is required for confirmation. The experimental
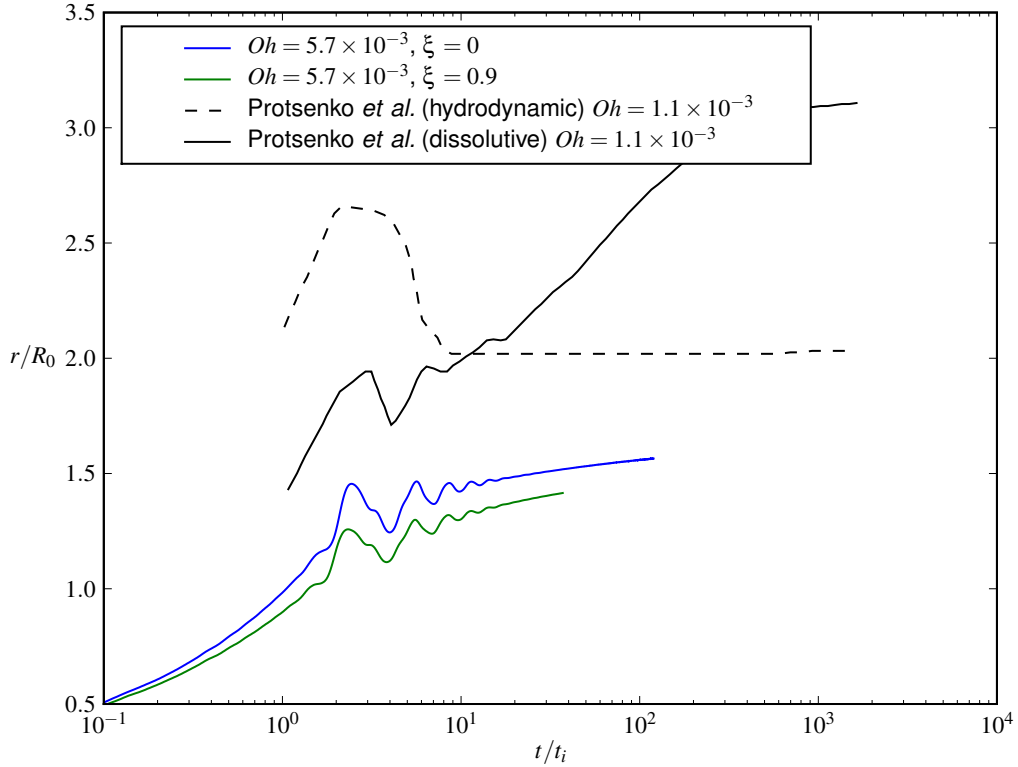
16

FIG. 7: The spreading radius versus time for the hydrodynamic case ($\xi = 0$) and a dissolutive case ($\xi = 0.9$, see Section IV for the definition of ξ). The black curves are Cu-Si experiments digitized from Protosenko *et al.*. The inertial time scale, t_i, for the Cu-Si system is calculated using $\rho = 8.9 \times 10^3$ kg/m^3, $\gamma = 1.3$ J/m^2 and $R_0 = 8.2 \times 10^{-4}$ m. The value of t_i is 1.9×10^{-8} s for this work and 2.0×10^{-3} s for the Cu-Si system

dissolutive and hydrodynamic cases (black curves) in Figure 7 clearly demonstrate oscillations of similar period, amplitude and duration to the simulation results as well as contact angle hysteresis. Oscillatory spreading also occurs in other systems such as water droplets on glass [18].

It has been conjectured [16, 17] that the value of λRe controls whether or not the spreading becomes oscillatory. In the simulations presented here, λRe varies between 1 and 10, but this is harder to determine for experimental systems. Hydrodynamic analysis of low temperature experimental data results in a slip length that can vary substantially for different materials (typically between 1 and 100 nm [7]). Using these bounds, the experimental
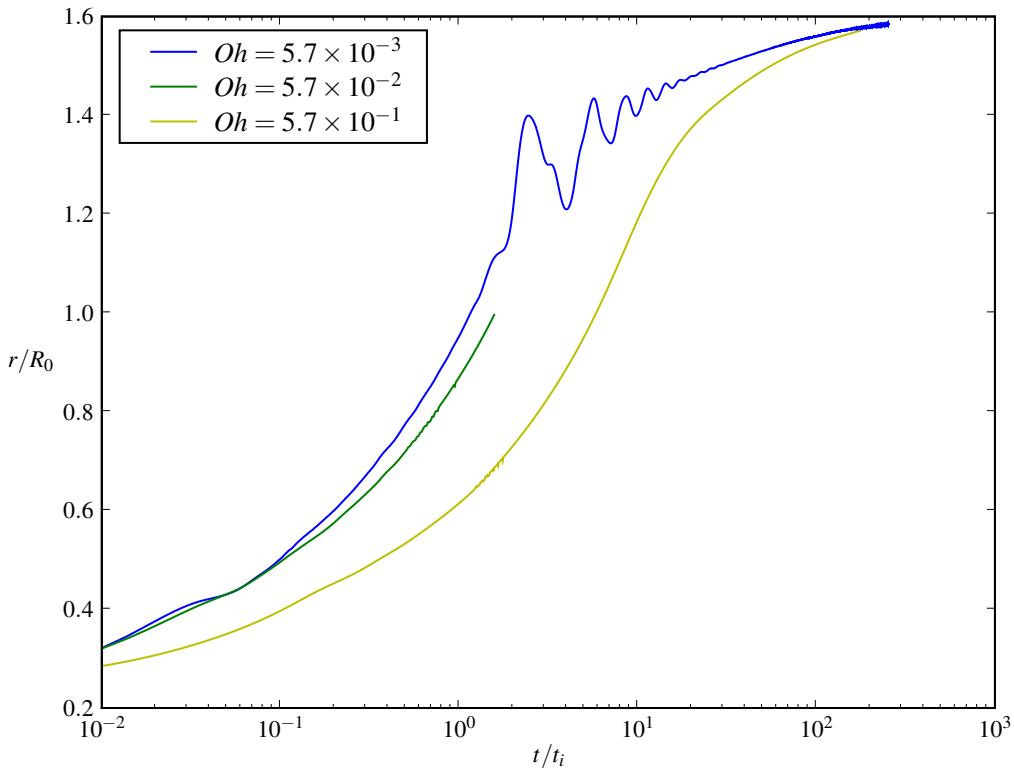
FIG. 8: The spreading radius versus time for various values of Oh. The smaller values of Oh converge to similar curves, but with varying oscillation durations. The oscillations are greatly reduced for the largest value of Oh.

systems results in, $0.01 < \lambda Re < 1$, assuming a spreading rate of 1 m/s (in this work the spreading rate is ≈ 10 m/s). It is interesting to note that for values of $\lambda Re < 0.1$, no oscillatory motion was seen in the work by Ding and Spelt [17]. In Schiaffino and Sorin [18] it is experimentally determined that the transition between under-damped oscillations to over-damped decay (no oscillations) occurs as Oh increases above 10^{-2}. This is seemingly confirmed in Figure 8 where the curve that corresponds to $Oh = 5.7 \times 10^{-3}$ has multiple oscillations, while the curve for $Oh = 5.7 \times 10^{-1}$ has no oscillations.

IV. DISSOLUTIVE SPREADING

In the previous section the hydrodynamic limit of a binary liquid was approximated by minimizing the driving force for dissolution. The initial concentration is now modified to

18

induce a driving force that promotes dissolution, while leaving the other initial conditions unchanged, and the consequences for spreading are discussed. In the simulations presented, a driving force for dissolution is established by decreasing the initial value of X_1^l, requiring the solid to melt in order to equilibrate the system. Explicitly, we set

$$X_1^l\left(t=0\right)=\left(1-\xi\right)X_1^{l,\mathrm{equ}}$$
$$\rho^l=\rho^{l,\mathrm{equ}}$$

(13)

where ξ is a measure of the magnitude of the driving force for dissolution ($\xi < 0$ induces freezing). In addition to the hydrodynamic base case ($\xi = 0$), simulations were conducted with values of $\xi = 0.5$ and $\xi = 0.9$.

The inertial spreading and dissolution time scales are vastly different resulting in only a small amount of dissolution during the simulations (the solid-fluid interface moves less than $\delta/5$). Nonetheless, the spreading dynamics are significantly influenced by the imposed concentration variations that determine the ultimate amount of dissolution. In general, dissolution is controlled by both boundary kinetics (here captured by t_ϕ) and bulk diffusion. Here $t_\phi \ll t_i$, thus dissolution will largely be controlled by bulk diffusion in the liquid. An approximate time scale for bulk diffusion mediated melting (dissolution) of a planar liquid-solid interface can be determined using an error function based similarity solution (see [30]). This time scale for the interface to move a distance δ is given by

$$t_{\mathrm{diff}}=\frac{\delta^2}{4K^2D}\approx 2.6\times 10^3 t_i$$

(14)

where K is the solution to

$$K+\left(\frac{X_1^l-X_1^{l,\mathrm{equ}}}{X_1^s-X_1^l}\right)\frac{\exp\left(-K^2\right)}{1-\mathrm{erf}\left(K\right)}\frac{1}{\sqrt{\pi}}=0$$

If we substitute R_0 for δ in Eq. (14) above, a rough estimate is obtained for complete equilibration of the system. Since $t_{\mathrm{diff}}\gg t_i$, the impact of dissolution on the geometric aspects of spreading in the simulations presented is negligible (the duration of the simulations is $\approx 100t_i$).

Results from the dissolutive simulations are presented in Figure 9. Perhaps surprisingly, both the rate of spreading and the extent of spreading are reduced as ξ is increased. This result agrees qualitatively with the experimental results from [9] shown in Figure 7. The saturated Cu-Si droplet (dashed curve) spreads further than the unsaturated Cu-Si droplet during the inertial regime.
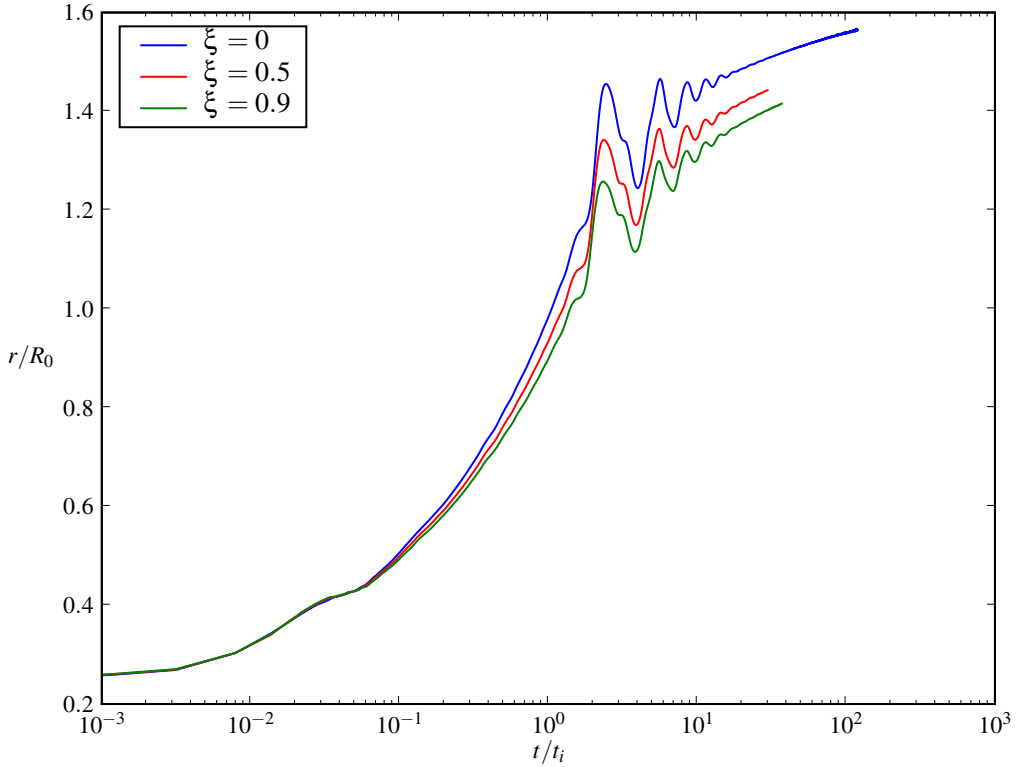
19

FIG. 9: The spreading radius versus time for various values of ξ. Clearly, as ξ increases, the spreading rate and extent of spreading is reduced.

The observed behavior in the simulations when $\xi > 0$ can be explained by an argument based on non-equilibrium interface energies, as is discussed in [7]. This argument postulates that spreading can be characterized by an instantaneous force balance at the triple line. This, in turn, requires knowledge of the instantaneous interface energies that are used to determine an intermediate non-equilibrium contact angle rather than the nominal $(t = \infty)$ equilibrium contact angle, θ^{equ}.

In order to make quantitative and test this hypothesis, we begin with two expressions for the equilibrium energy of a planar interface:

$$\gamma = \int_{-\infty}^{\infty} \left[\epsilon_1 T |\nabla \rho_1|^2 + \epsilon_2 T |\nabla \rho_2|^2 + \epsilon_\phi T |\nabla \phi|^2 \right] dl = 2 \int_{-\infty}^{\infty} \left[f - f^\infty - \mu_i^\infty \left(\rho_i - \rho_i^\infty \right) \right] dl \quad (15)$$

where the ∞ superscript represents the value in the far field, and all the fields have equilibrium profiles . We now assert that a plausible measure of the instantaneous interface energy

is

$$\tilde{\gamma}(t) = \int_l \left[\epsilon_1 T |\nabla \rho_1|^2 + \epsilon_2 T |\nabla \rho_2|^2 + \epsilon_\phi T |\nabla \phi|^2 \right] dl \qquad (16)$$

where $l > \delta$ is a line that both intersects and is normal to the interface being measured, and all fields are measured at time t. In general, the quantity $\tilde{\gamma}$ is a useful heuristic when the gradients are confined to the interface region. The numerical integration of Eq. (16) is conducted at a distance of 2δ from the triple-line location perpendicular to each local interface over a distance of 1.5δ. The integration points on the respective interfaces are chosen to be as near to the triple-line location as possible while avoiding the large variations in the value of $\tilde{\gamma}$ that occur close to the triple-line location (see Figure 10). Clearly, we could have defined another surface energy,

$$\gamma^*(t) = 2 \int \left[f - f^\infty - \mu_i^\infty (\rho_i - \rho_i^\infty) \right] dl \qquad (17)$$

As one approaches equilibrium $\gamma^* \to \tilde{\gamma}$, but in general the quantities are different. It would appear that γ^* is less useful than $\tilde{\gamma}$, as γ^* requires the fields to be near the far field (equilibrium) values at the integration limits extremes for the value to "make sense" as an interface excess quantity.

Using our definition of $\tilde{\gamma}$, we can now define a new contact angle $\theta_d(t)$ based on a postulated instantaneous force balance at the triple-line. Using Young's Equation, we propose

$$\theta_d(t) = \arccos\left(\frac{\tilde{\gamma}_{sv}(t) - \tilde{\gamma}_{sl}(t)}{\tilde{\gamma}_{lv}(t)} \right) \qquad (18)$$

Because the solid-fluid interface is planar over the time scales of interest we may use Eq. (18) instead of the more general Neumann's triangle horizontal and vertical force balance.

In Figure 11, θ_d is displayed alongside the actual or measured contact angle, θ_a, for each value of ξ simulated. Figure 11 demonstrates two interesting features. Firstly, at early times, when $t < 0.1t_i$, the difference between θ_a and θ_d decreases with increasing ξ and, secondly, at longer times, θ_d and θ_a correspond quite closely. The first feature indicates that the difference between θ_a and θ_d can be viewed as an initial driving force for spreading. The greatest extent of spreading occurs for $\xi = 0$, which has the largest value of the quantity $\theta_a - \theta_d$ consistent with this hypothesis. The near correspondence of θ_a and θ_d, indicates that the evolution of θ_d controls the spreading.

Since θ_d is derived from the $\tilde{\gamma}$, it is instructive to observe the $\tilde{\gamma}$ behavior over time (see Figure 12). The values of $\tilde{\gamma}$ differ substantially from their equilibrium values. The $\tilde{\gamma}_{sv}$
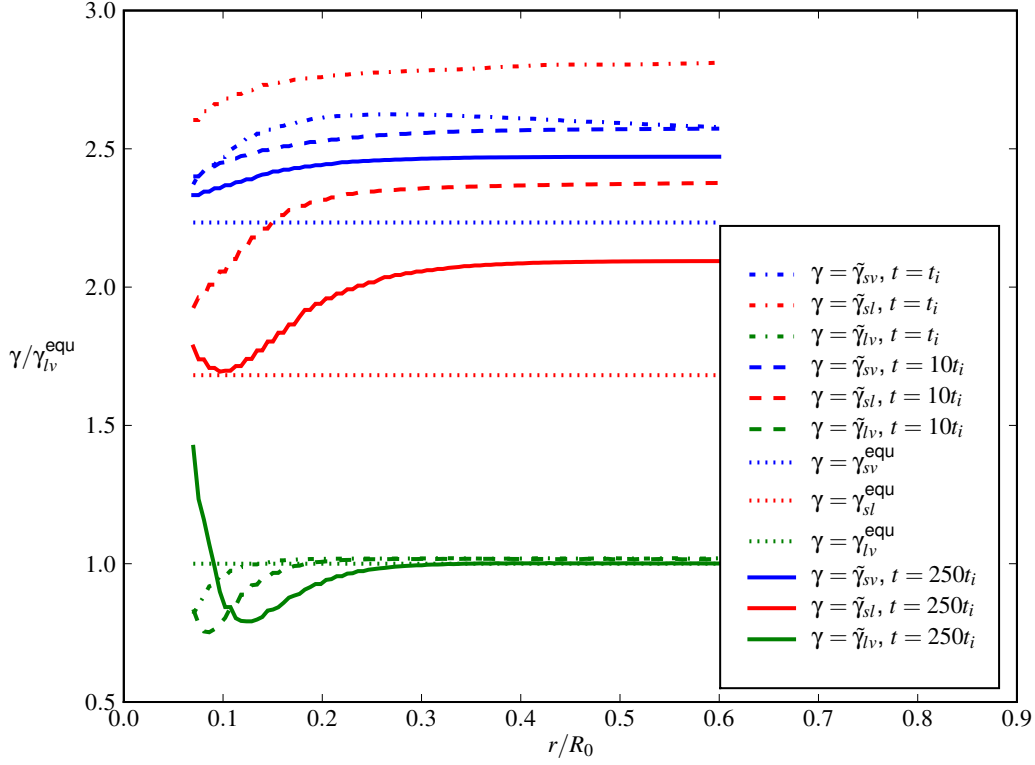
FIG. 10: The values of the instantaneous interface energies, $\tilde{\gamma}$, at positions moving away from the moving triple-line location for $\xi = 0$ at times $t = t_i$ and $t = 10t_i$ and $t = 250t_i$. The $\tilde{\gamma}_{lv}$ is in reasonable agreement with the equilibrium value, while the values of $\tilde{\gamma}_{sl}$ and $\tilde{\gamma}_{sv}$ decrease slowly to their equilibrium values, see Figure 12.

are independent of ξ, which is a reasonable expectation, as ξ sets the liquid concentration. Increasing ξ from the hydrodynamic case to $\xi = 0.9$ results in an increase in $\tilde{\gamma}_{lv}$ and $\tilde{\gamma}_{sl}$. This increase results in a decrease in the unbalanced force at the triple-line, explaining the observed decrease in the spreading rate.

The adjustment to the equilibrium interface conditions is extremely complex and intimately related to the interface width and the interpolated values of the dynamic coefficients (ν and $\bar{M}$), see Eqs. (5) and (6). The choice for the interpolation parameter a in Eqs. (5) and (6) biases the coefficients to have values close to the bulk fluid values in the interface region enabling the fastest adjustment to local equilibrium within the bounds set by the bulk values. The parameter a is tuned to a value of 4, as below this value, test simulations
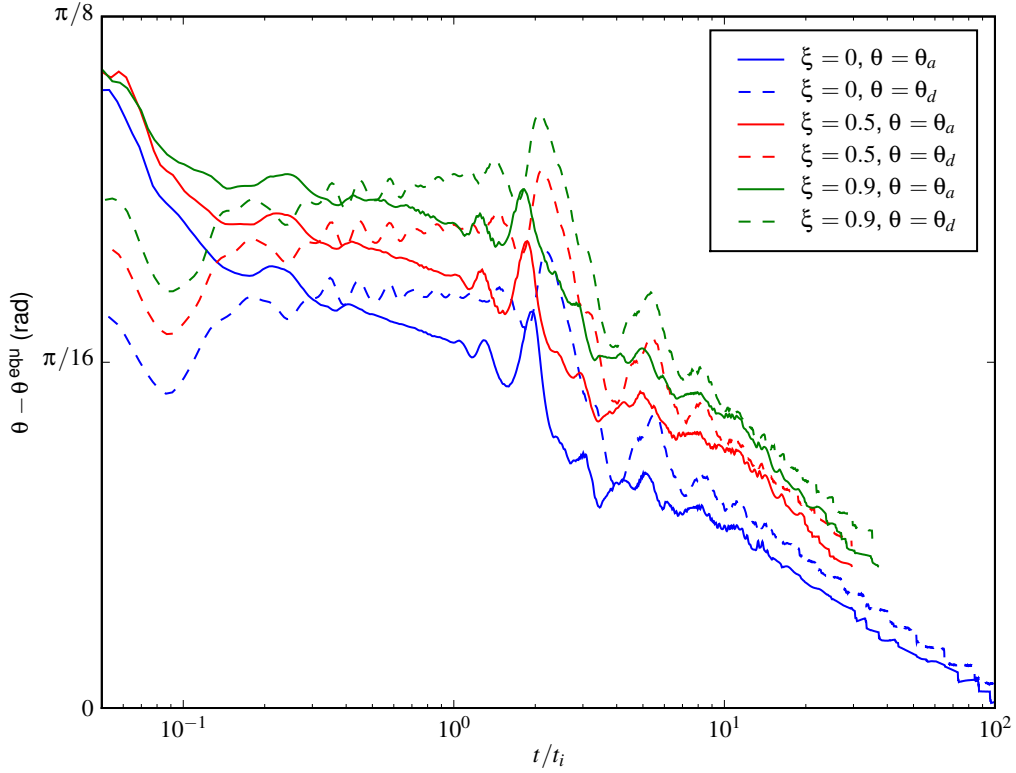
FIG. 11: The measured contact angle (θ_a) and the contact angle derived from the $\tilde{\gamma}$ (θ_d) versus time for various values of ξ. For each value of ξ, the angle θ is largely independent of θ_d when $t < t_i$, but become more aligned as t increases. The reduced value of $\theta_a - \theta_d$ as ξ increases corresponds to decreased spreading rates.

showed a considerable reduction in the local interface equilibration rate.

The adjustment of the interface profiles due to hydrodynamics is fast, evidenced by the comparatively rapid local equilibration of the density profile across the interface regions (not shown here). The adjustment of the concentration profile through the interface is slower, requiring inter-diffusion between the bulk phases and the interface regions. This compositional relaxation could, in principle, be as slow as the diffusion time scale, t_{diff} (see Eq. (14)), although the connection is imprecise, as this quantity is associated with the motion of the interface due to dissolution (melting) rather than the relaxation of compositional profiles within the interface. The solid interfaces equilibrate slowly, compared to the liquid-vapor interface, as seen in Figures 10 and 12. We expect that the observed interface relaxation
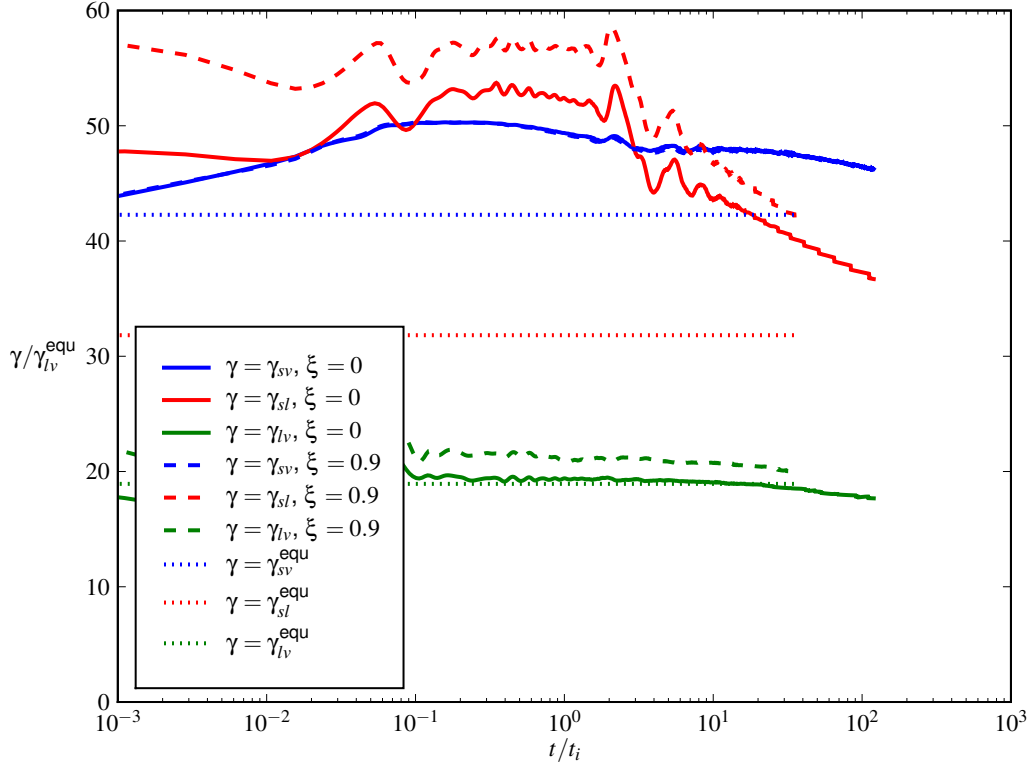
FIG. 12: The instantaneous interface energies $\tilde{\gamma}$ plotted against time for both the dissolutive and non-dissolutive cases. The dissolutive case has greater values of both $\tilde{\gamma}_{lv}$ and $\tilde{\gamma}_{sl}$, which leads to retarded spreading. The values of $\tilde{\gamma}$ are calculated by numerically integrating Eq. (16) at a distance of 2 δ from the triple-line location perpendicular to the local interface across a distance of 1.5 δ.

time is unrealistic, when compared with experimental studies of metallic systems, as our chosen interface interface width of $\delta = 100$ nm is much larger than the $\delta \approx 1$ nm typical of metals. This is a known shortcoming of this treatment, and certainly results in an unphysical time scale for local interface equilibration. Further analysis of the relationship between δ and the equilibration rate is required, though this analysis is beyond the scope of this work. The limitation of requiring $\delta/R \approx 0.1$ imposed by the available computation resources does not detract from the analysis presented in Sections III and IV with respect to the reduced spreading when ξ is increased, the qualitative description of the spreading regimes and oscillations, or the quantitative comparisons with experiments.

24

A. Dissipation

Much of the literature surrounding droplet spreading is concerned with characterizing dissipation mechanisms from the point of view of an irreversible thermodynamic process [7, 31, 32]. In this spirit, this section provides an analysis of the entropy production, yielding the magnitudes of the various dissipation mechanisms in our model, which should, in turn, provide guidance on the formulation of simplified models. The expression used here for the total entropy production rate is given by [33],

$$\dot{S}_{\text{PROD}} = \frac{M}{T^2} |\partial_j \left(\mu_1^{\text{NC}} - \mu_2^{\text{NC}} \right)|^2 + \frac{M_\phi}{T^2} \left(\frac{\partial f}{\partial \phi} - \epsilon_\phi T \partial_j^2 \phi \right)^2 + \frac{\nu}{2T} \left(\partial_i u_k + \partial_k u_i \right) \partial_i u_k \qquad (19)$$

where each term in the sum is a distinct dissipation mechanism (diffusion, solid interface relaxation, and viscous flow).

The comprehensive overview by de Gennes [31] identified three main mechanisms for dissipation in spreading droplets: a viscous dissipation concerned with the "rolling motion" of the fluid within 100 μm of the triple line, a viscous dissipation in the precursor film and a highly localized dissipation at the triple line associated with "triple-line friction". In the present work, the precursor film is absent, as the short range van der Waals interactions responsible for the film are not included in the model. However, both viscous dissipation in the bulk fluid and local triple-line dissipation are present, but are conflated within the viscous dissipation term in Eq. (19). In most models of droplets spreading, the chosen model for slip relaxation at the triple line influences the underlying dissipation mechanism for the spreading droplet. For example, a molecular kinetics model of slip generally implies a local triple-line dissipation, while a hydrodynamic model of slip, such as Cox's model [34] or Tanner's law [29], both examples of de Gennes' "rolling motion", implies non-localized dissipation [7, 32]. We are reminded that this model employs diffuse interfaces, and thus no explicit slip condition is postulated, but such slip is a direct consequence of the model.

Figure 13 presents color contour plots of the entropy production rates at various times. The plots show the magnitude, location and mechanism of entropy production for the non-dissolutive case (the dissolutive cases are only slightly different). The color mapping is rescaled in Figure 13 based on the $\max \left(\dot{S}_{\text{PROD}} \right)$ value for each image. For example, the total entropy production rate in Figure 13 (d) is only 0.4% of the value in Figure 13 (a). If we were considering a non-isothermal system, there would be a further term in expression 19
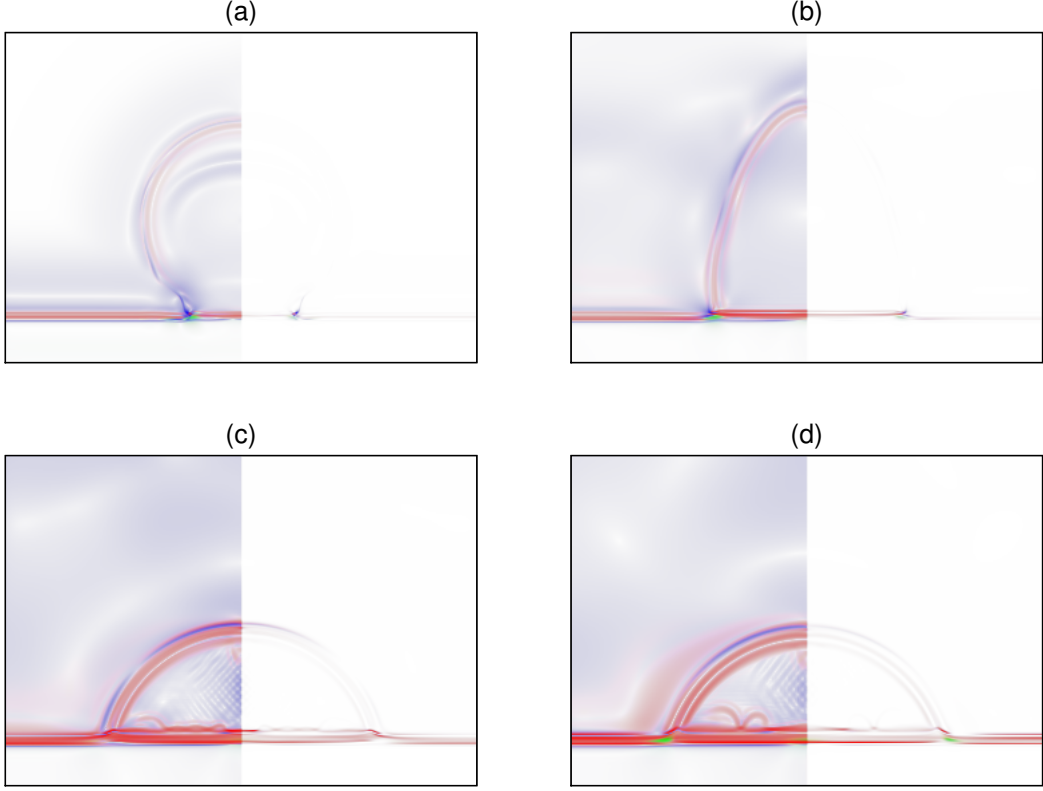
FIG. 13: Contour plots of the entropy production rate at (a) $t = 0.1t_i$, (b) $t = t_i$, (c) $t = 10t_i$ and (d) $t = 20t_i$. The color intensity represents the magnitude of either $\sqrt[8]{\dot{S}_{\text{PROD}}}$ (less focused) on the left panel or $\sqrt{\dot{S}_{\text{PROD}}}$ (more focused) on the right panel. The colors represent the specific entropy production mechanism given by the terms in Eq., (19), with red, green and blue representing the first (diffusion), second (solid interface relaxation) and third (viscous flow) terms, respectively.

containing temperature gradients, an effect not considered in this work.

At very early times (not shown), the entropy production is highly localized at the solid-fluid interface region as ϕ locally equilibrates. Subsequently (not shown), pressure waves are observed as the liquid-vapor interface equilibrates, and viscosity is the dominant mode of dissipation. By $t = 0.1t_i$, the pressure waves have mostly subsided and the spreading is well under way. At this stage, the dominant dissipation mechanism remains viscous but is now highly localized at the triple-line. As the inertial time scale is approached in Figure 13 (b), the dominant mechanism alternates between diffusive and viscous as the droplet oscillates during the $t_i < t < 10t_i$ stage. The viscous dissipation remains highly localized at the

triple line, while the diffusive dissipation mostly occurs in the solid-liquid interface with some occurring along the solid-vapor interface. This correlates with Figure 12, which shows that the solid-liquid interface is far from local equilibrium until much later times. At later times (Figure 13 (c)), dissipation is mainly due to local interface equilibration along the solid-liquid and solid-vapor interface regions. The proportion of the numerically integrated value of $\int \dot{S}_{\text{PROD}} dV$ for each term in Eq. (19) is (a) (0.51, 0.06, 0.43), (b) (0.73, 0.04, 0.23), (c) (0.84, 0.02, 0.14) and (d) (0.85, 0.07, 0.08) for each subplot in Figure 13. These proportions demonstrate the growing influence of diffusive dissipation and the reduction in viscous dissipation as the system transitions from the inertial regime to the diffusive regime.

V. CONCLUSION

This paper presents results from a model of dissolutive spreading simulated in a parameter regime where inertial effects are initially dominant. The triple-line motion demonstrates good agreement with the $O(t^{-1/2})$ inertial spreading rate. The model also generates oscillations characteristic of the transition from inertial to viscous or diffusive spreading. Subsequent analysis indicates that a force balance involving the instantaneous interface energies evaluated using the expression in Eq. (16) can explain the variation in spreading between the hydrodynamic and dissolutive cases. At late times, after inertial effects have ceased, the contact angle derived from the instantaneous interface energies is within 0.005 rad of the measured contact angle suggesting that the local interface equilibration mechanism is controlling the spreading. Analysis of the dissipation mechanism via the entropy production expression demonstrates that dissipation occurs at the triple line during the inertial stage, but transitions to the solid-fluid interfaces during the oscillatory stage consistent with the instantaneous interface energy analysis. Overall, the simulation results show good quantitative and qualitative agreement with a number of experimental results when time is scaled with the inertial time scale.

Modeling droplets that have both a realistic interface width and include inertial effects is impractical with current computational resources (at least for the model presented herein) and may require years of real time computation on large parallel clusters. In this work, to reduce the required compute time, the use of a realistic interface width has been sacrificed in order to preserve the inertial effects. This has the consequence of increasing the simulation

time required for the local equilibration process across the solid-fluid interface as discussed in Section IV. Although, this process has a longer duration than physically appropriate in the present work, a time regime over which the controlling mechanism for spreading is the local interface equilibration may be entirely physical. It is noted in Protsenko *et al.* [9] that the diffusive stage may occur in two separate parts. The first part is surmised to be the solid-liquid interface equilibration process and takes approximately an order of magnitude longer than the inertial time scale, which is faster than occurs here, but very similar in nature. The second part is the melting of the substrate, which is included in this model, but not observed as it occurs over a time scale longer than the total duration of a typical simulation.

Further work may involve both direct comparison with molecular kinetics theory and more detailed analysis of the impact of the interface width on the spreading dynamics.

VI.   ACKNOWLEDGEMENTS

[1] J. A. Warren, W. J. Boettinger, and A. R. Roosen, Acta Materialia **46**, 3247 (1998), ISSN 1359-6454, URL `http://www.sciencedirect.com/science/article/B6TW8-3TTV5KB-2T/2/9c0fb5ccb7ad4e0c546b9b19365ee505`.

[2] W. Villanueva, K. Grönhagen, G. Amberg, and J. A. gren, Physical Review E (Statistical, Nonlinear, and Soft Matter Physics) **77**, 056313 (pages 13) (2008), URL `http://link.aps.org/abstract/PRE/v77/e056313`.

[3] S. Su, L. Yin, Y. Sun, B. T. Murray, and T. J. Singler, ACTA MATERIALIA **57**, 3110 (2009), ISSN 1359-6454.

[4] W. Villanueva, W. J. Boettinger, J. A. Warren, and G. Amberg, ACTA MATERIALIA **57**, 6022 (2009).

[5] E. Saiz, A. Tomsia, and R. Cannon, ACTA MATERIALIA **46**, 2349 (1998), ISSN 1359-6454, 3rd International Workshop on Interfaces, SANTIAGO COMPOSTE, SPAIN, SEP, 1996.

[6] R. Voitovitch, A. Mortensen, F. Hodaj, and N. Eustathopoulos, ACTA MATERIALIA **47**, 1117 (1999), ISSN 1359.

[7] E. Saiz and A. Tomsia, NATURE MATERIALS **3**, 903 (2004), ISSN 1476-1122.

[8] G. N., V. Poluyanskaya, N. Eustathopoulos, and Y. Naidich, NATO ASI SERIES 3 HIGH TECHNOLOGY **58**, 57 (1998).

[9] P. Protsenko, O. Kozova, R. Voytovych, and N. Eustathopoulos, JOURNAL OF MATERIALS SCIENCE **43**, 5669 (2008), ISSN 0022-2461.

[10] L. Yin, B. T. Murray, S. Su, Y. Sun, Y. Efraim, H. Taitelbaum, and T. J. Singler, JOURNAL OF PHYSICS-CONDENSED MATTER **21** (2009), ISSN 0953-8984.

[11] E. Saiz, A. P. Tomsia, N. Rauch, C. Scheu, M. Ruehle, M. Benhassine, D. Seveno, J. de Coninck, and S. Lopez-Esteban, PHYSICAL REVIEW E **76** (2007), ISSN 1539-3755.

[12] E. Saiz, R. Cannon, and A. Tomsia, ACTA MATERIALIA **48**, 4449 (2000), ISSN 1359, Acta Materialia Workshop on Ceramic and Biomaterial Interfaces: Designing for Properties, SEVILLE, SPAIN, SEP 20-23, 1999.

[13] A.-L. Biance, C. Clanet, and D. Quéré, Phys. Rev. E **69**, 016301 (2004).

[14] E. B. W. III, G. S. Grest, D. R. Heine, and J. Hoyt, Acta Materialia **53**, 3163 (2005), ISSN 1359-6454, URL `http://www.sciencedirect.com/science/article/B6TW8-4G1R42V-1/2/4e39027a84a0767aad2aaa3b612551d2`.

[15] Y. Sun and E. B. W. III, Journal of Physics: Condensed Matter **21**, 464135 (13pp) (2009), URL `http://stacks.iop.org/0953-8984/21/464135`.

[16] L. Hocking and S. Davis, JOURNAL OF FLUID MECHANICS **467**, 1 (2002), ISSN 0022-1120.

[17] H. DING and P. D. M. SPELT, Journal of Fluid Mechanics **576**, 287 (2007).

[18] S. Schiaffino and A. Sonin, PHYSICS OF FLUIDS **9**, 3172 (1997), ISSN 1070.

[19] D. JACQMIN, Journal of Fluid Mechanics **402**, 57 (2000), URL `http://journals.cambridge.org/action/displayAbstract?fromPage=online&aid=15613&fulltextType=RA&fileId=S0022112099006874`.

[20] Acta Materialia **54**, 3561 (2006), selected Papers from the Meeting.

[21] M. Schneemilch, R. Hayes, J. Petrov, and J. Ralston, LANGMUIR **14**, 7047 (1998), ISSN

0743.

[22] J. E. Guyer, D. Wheeler, and J. A. Warren, Computing in Science & Engineering **11**, 6 (2009), URL http://link.aip.org/link/?CSX/11/6/1.

[23] Reactive Wetting Code Installation, URL http://www.ctcms.nist.gov/fipy/reactiveWetting.html.

[24] M. A. Heroux, R. A. Bartlett, V. E. Howle, R. J. Hoekstra, J. J. Hu, T. G. Kolda, R. B. Lehoucq, K. R. Long, R. P. Pawlowski, E. T. Phipps, et al., ACM Trans. Math. Softw. **31**, 397 (2005), ISSN 0098-3500.

[25] Certain trade names and company products are mentioned in the text or identified. In no case does such identification imply recommendation or endorsement by the National Institute of Standards and Technology (NIST), nor does it imply that the products are necessarily the best available for the purpose.

[26] M. Plischke and B. Bergersen, *Equilibrium statistical physics* (World Scientific, 1994).

[27] W. J. Boettinger, J. A. Warren, C. Beckermann, and A. Karma, Annual Review of Materials Research **32**, 163 (2002), URL http://arjournals.annualreviews.org/doi/abs/10.1146/annurev.matsci.32.101901.155803.

[28] L. D. Landau and E. M. Lifshitz, *Fluid Mechanics*, vol. 6 of *Course in Theoretical Physics* (Pergamon Press, 1987), 2nd ed., translated from the Russian by J. B. Sykes and W. H. Reid.

[29] L. TANNER, JOURNAL OF PHYSICS D-APPLIED PHYSICS (????).

[30] W. J. Boettinger and G. B. McFadden, *Bending of a bimetallic beam due to the kirkendall effect*, in preperation.

[31] P. G. de Gennes, Rev. Mod. Phys. **57**, 827 (1985).

[32] F. Brochard-Wyart and P. de Gennes, Advances in Colloid and Interface Science **39**, 1 (1992), ISSN 0001-8686, URL http://www.sciencedirect.com/science/article/B6V5F-44MRRDT-1F/2/8733966fafa2268761ea972ba387183e.

[33] R. SEKERKA and Z. BI, Interfaces for the 21st century: new research directions in fluid mechanics and materials science: a collection of research papers dedicated to Steven [ie Stephen] H. Davis in commemoration of his 60th birthday p. 147 (2002).

[34] R. COX, JOURNAL OF FLUID MECHANICS (????).

[35] C. Kittel and H. Kroemer, *Thermal physics* (WH Freeman & Co, 1980).

[36] Z. Bi and R. F. Sekerka, Physica A: Statistical and Theoretical Physics **261**, 95 (1998), ISSN

0378-4371, URL `http://www.sciencedirect.com/science/article/B6TVG-3VCDM20-9/2/6670ccfc4b96d8325d107ebd3a2beb8d`.

[37] D. Anderson, G. McFadden, and A. Wheeler, ANNUAL REVIEW OF FLUID MECHANICS **30**, 139 (1998).

[38] J. H. Ferziger and M. Perić, *Computational Methods for Fluid Dynamics* (Springer, 1996).

[39] C. M. Rhie and W. L. Chow, AIAA Journal **21**, 1525 (1983).

[40] D. Jamet, D. Torres, and J. U. Brackbill, Journal of Computational Physics **182**, 262 (2002).

[41] M. Heroux, R. Bartlett, V. H. R. Hoekstra, J. Hu, T. Kolda, R. Lehoucq, K. Long, R. Pawlowski, E. Phipps, A. Salinger, et al., Tech. Rep. SAND2003-2927, Sandia National Laboratories (2003), URL `http://trilinos.sandia.gov/`.

[42] I. J. Keshtiban, F. Belblidia, and M. F. Webster, Tech. Rep. (2004), URL `http://www.cs.swan.ac.uk/reports/yr2004/CSR2-2004.pdf`.

Appendix A: Derivation of the Governing Equations

In this section the underlying thermodynamic and constitutive relationships required for the derivation of Eqs. (2), (3) and (4) are presented.

As previously outlined, the fluid phases are represented by a binary, van der Waals equation of state and the solid phase is represented by a simple linear compressive and tensile equation of state that ignores all shear stress. The van der Waals equation of state is given by,

$$\left(P - \frac{n^2}{V^2} \left(e_1 X_1 + e_2 X_2 \right) \right) (V - \bar{v}n) = nRT \tag{A1}$$

where X_1 and X_2 are the concentrations of each component, n is the number of moles and $V/n = m/\rho$. All other parameters used in Eq. (A1) are defined in Section II. Eq. (A1) can be related to the ideal gas law, but has a modified pressure and volume term to account for the long range attraction of molecules and volume exclusion, respectively [26, 35]. The solid equation of state is given by,

$$PV_s = 2Bn \frac{V_s - V}{V_s} \tag{A2}$$

where $V_s/n = m/\rho_s^{\text{ref}}$. The Helmholtz free energies given in Eqs. (II 4) and (7) are derived from (A1) and (A2), respectively, using the thermodynamic identities given in Eqs. (8), (9) and (10). In order to derive Eqs. (2), (3) and (4), it is necessary to postulate a form for the

31

free energy functional.

As in reference [36], standard non-classical diffuse interface expressions for ρ_1, ρ_2 and ϕ are used, which results in a functional of the form,

$$F = \int \left[f + \frac{\epsilon_\phi T}{2}|\nabla\phi|^2 + \frac{\epsilon_1 T}{2}|\nabla\rho_1|^2 + \frac{\epsilon_2 T}{2}|\nabla\rho_2|^2 \right] dV$$

Using standard dissipation arguments [36], Eqs. (2) and (3) are derived using,

$$\frac{D\phi}{Dt} = -M_\phi \frac{\delta F}{\delta\phi}$$

and

$$\frac{\partial\rho_i}{\partial t} + \partial_j\left(u_j\rho_i\right) = -\partial_j J_{ij}$$

The fluxes are given by,

$$J_{1j} = -J_{2j} = -M\partial_j \left(\frac{\mu_1^{NC} - \mu_s^{NC}}{T} \right)$$

where,

$$\mu_1^{NC} = \frac{\delta F}{\delta\rho_1}$$

and

$$\mu_2^{NC} = \frac{\delta F}{\delta\rho_2}$$

The form of the stress tensor required to derive the momentum equation is given by,

$$\sigma_{ij} = \nu\left(\partial_j u_i + \partial_i u_j\right) + t_{ij}$$

using the standard assumption that the bulk viscosity, λ, is related to the shear viscosity via $\lambda = -\frac{2}{3}\nu$. The tensor, t_{ij}, is derived from a conservation law ($\partial_j t_{ij} = 0$) based on Noether's theorem [37]. The expression for t_{ij} is given by,

$$t_{ij} = g^{NC}\delta_{ij} - \partial_j\rho\frac{\partial g^{NC}}{\partial\left(\partial_i\rho\right)} \tag{A3}$$

where

$$g^{NC} = f^{NC} + \rho_1\lambda_1 + \rho_2\lambda_2 \tag{A4}$$

The quantity g^{NC} is the form of the free energy that includes Lagrange multipliers for conservation of species 1 and 2. The Lagrange multipliers for each species are equal to $\lambda_1 = -\mu_1^{NC}$ and $\lambda_2 = -\mu_2^{NC}$ in equilibrium using the variational derivative of $\int g^{NC}dV$ with respect to ρ_1 and ρ_2. Using Eqs. (A3) and (A4) the form for $\partial_i t_{ij}$ used in Eq. (4) can be derived,

$$\partial_j t_{ij} = -\rho_1\partial_i\mu_1^{NC} - \rho_2\partial_i\mu_2^{NC} - \partial_i\phi\frac{\delta F}{\delta\phi} \tag{A5}$$

Appendix B: Numerical Approach

In general, even for compressible systems, many conventional algorithms use the pressure field as the independent variable rather than the density field. This approach is thought to have more robust convergence properties [38] at low Mach numbers due to the weak dependence of pressure gradients on density, but the convergence properties deteriorate at higher Mach numbers. In this work, due to the non-trivial nature of the pressure-density relationship, an inversion of this relationship would be impractical and it is more natural to solve for the density field rather than the pressure field. The convergence issues will be addressed further in the following sections. Due to the mesh collocation of the density and velocity fields, an interpolation scheme, known as Rhie-Chow interpolation [39], is employed to ensure adequate velocity-pressure coupling.

1. Parasitic Currents

Parasitic currents are a common source of numerical errors when computing flows with interface energy driving forces that have large Ca. Typically, for the systems of interest in this paper, $Ca \approx 10^{-2}$, but parasitic velocities were still found to be a source of numerical error particularly when trying to evaluate equilibrium solutions. Parasitic currents are characterized by quasi-steady flow fields that do not dissipate over time despite the system reaching equilibrium in all other respects. This can result in equilibrium errors in both the density and concentration fields. Jamet *et al.* [40] as well as other researchers have demonstrated that parasitic currents can be eliminated by recasting the momentum equation in a form that only conserves momentum to the truncation error of the discretization rather than machine precision. The form of the momentum equation that eliminates parasitic currents is written in terms of the chemical potentials and is given by,

$$\frac{\partial \left(\rho u_i \right)}{\partial t} + \partial_j \left(\rho u_i u_j \right) = \partial_j \left(\nu \left[\partial_j u_i + \partial_i u_j \right] \right) - \rho_1 \partial_i \mu_1^{NC} - \rho_2 \partial_i \mu_2^{NC} \qquad \text{(B1)}$$

The discretized form of Eq. (B1) is known as an energy conserving discretization in contrast to the momentum conserving discretization, which results when the momentum equation is written in terms of the pressure.

2. Convergence

Some simulations in this paper are tested for convergence with grid sizes of $180{\times}125$, $360{\times}250$ and $720{\times}500$ using the triple-line and drop height positions against time as the metrics for convergence. Production runs for the results presented use $360{\times}250$ grids. Details of these convergence test can be found in ref [23]. Convergence at the nth time-step is achieved when the kth iteration within the time step satisfies the residual condition $\beta_n^k/\beta_n^0 < 1 \times 10^{-1}$ for both the continuity and momentum equations using the L2 norm. Further decreases in the residual made little difference to the dynamic positions of the drop height and triple-line. Numerical calculations indicate that Ma values vary between intervals where $Ma > 2 \times 10^{-1}$ that require compressible flow solvers (density based) and intervals where $Ma < 2 \times 10^{-1}$ for which compressible flow solvers have trouble with accuracy and convergence for traditional segregated solvers. The shift to low Ma generally occurs when the system is quite close to equilibrium and is not believed to effect the dynamic aspects of the simulation, which are of most interest in this paper. In general, for low Mach number flows, preconditioners are used to improve the convergence properties of segregated solvers. In this work it was found that using a coupled solver along with a suitable preconditioner greatly improved the convergence properties. The preconditioners are available as part of the Trilinos software suite [41]. The coupled convergence properties can be further improved by employing physics based preconditioners that change the nature of the equations based on the value of Ma [42], but are not used in this work. The temporal and spatial convergence tests conducted showed adequate convergence for the macroscale effects such as triple line motion, which are of interest here (see [23] for details).